

# End-To-End Convolutional Neural Network for 3D Reconstruction of Knee Bones From Bi-Planar X-Ray Images

Yoni Kasten<sup>\*1,2</sup>, Daniel Doktovsky<sup>\*1</sup>, and Ilya Kovler<sup>\*1</sup>

<sup>1</sup> RSIP Vision

<sup>2</sup> Weizmann Institute of Science

**Abstract.** We present an end-to-end Convolutional Neural Network (CNN) approach for 3D reconstruction of knee bones directly from two bi-planar X-ray images. Clinically, capturing the 3D models of the bones is crucial for surgical planning, implant fitting, and postoperative evaluation. X-ray imaging significantly reduces the exposure of patients to ionizing radiation compared to Computer Tomography (CT) imaging, and is much more common and inexpensive compared to Magnetic Resonance Imaging (MRI) scanners. However, retrieving 3D models from such 2D scans is extremely challenging. In contrast to the common approach of statistically modeling the shape of each bone, our deep network learns the distribution of the bones' shapes directly from the training images. We train our model with both supervised and unsupervised losses using Digitally Reconstructed Radiograph (DRR) images generated from CT scans. To apply our model to X-Ray data, we use style transfer to transform between X-Ray and DRR modalities. As a result, at test time, without further optimization, our solution directly outputs a 3D reconstruction from a pair of bi-planar X-ray images, while preserving geometric constraints. Our results indicate that our deep learning model is very efficient, generalizes well and produces high quality reconstructions.

**Keywords:** 3D reconstruction · X-ray imaging · Deep Learning · Patient specific planning

## 1 Introduction

3D reconstruction of knee bones is an important step for various clinical applications. It may be used for surgical planning, precise implant selection, patient specific implant manufacturing or intraoperative jig printing which perfectly fits the anatomy. X-ray images are often used due to their wide availability, lower price, short scanning time and lower levels of ionizing radiation compared to CT scanners. However, since X-ray images provide only

---

\*Equal contributors

This work has been done at RSIP Vision

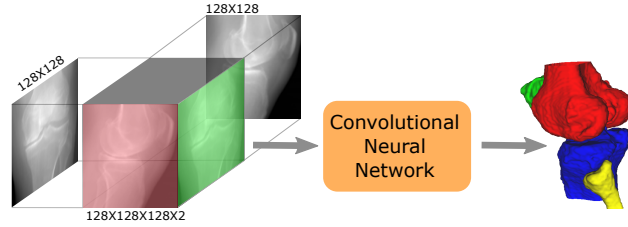


Fig. 1: General scheme: AP and lateral X-ray scans of the knee joint are replicated into a 3D array, each on a different channel (green and red for illustration). A CNN then predicts a 3D segmentation map of the bone classes which is used for 3D reconstruction of the bones.

2D information, some prior knowledge must be incorporated in order to extract the missing dimension. Previous approaches [5,17,8,7] use Statistical Shape Models (SSM) or Statistical Shape and Intensity Models (SSIM) for reconstructing bones from X-ray images. However, optimization for the deformable model parameters might be slow and needs a good initialization point to avoid local maxima [22,15].

In this paper, we present a novel end-to-end deep learning approach for 3D reconstruction of knee joints from two bi-planar X-ray images. The overall scheme is presented in Fig. 1. CNNs have recently proven very effective for various types of tasks [18], including image segmentation and classification. However, implementing 3D reconstruction from two or more 2D images using a deep learning approach remains a challenging task, due to the difficulty of representing a dimensional enlargement in multi-view settings with standard differentiable layers. Moreover, due to the transparent nature of X-ray images, matching surface points between multi-views for dense reconstruction is extremely challenging compared to the standard multi-view setting [11].

We address these challenges by introducing a dimensional enlargement approach that given two bi-planar X-rays back-projects each pair of corresponding epipolar lines into a two-channeled epipolar plane. This results in a 3D volume that contains all the information observed from the two X-ray images, while preserving the two-view geometric constraints. We combine this representation with a deep learning architecture that outputs 3D models of the different bones. The experiments show the utilization of our approach for 3D reconstruction of knee joint. We strongly believe that our method paves the way for future research in deep learning based 3D modeling of bones from X-ray scans. In contrast to SSM based methods, our method does not require an initialization and runs in 0.5 seconds while a standard SSM optimization for one knee bone takes about 4.88 seconds.

## 2 Related work

**Deformable models** 3D bones reconstruction from X-ray images is mostly done by SSM [5,17,6,1] for bones surface modeling, or SSIM[8,7] for further modeling bones interior density. We refer the readers to [22,9] for comprehensive overviews of the existing methods. The basic principle is to rigidly align a collection of 3D models and to characterize their non-rigid mutual principal components. Then, given one or more X-ray images, a 3D reconstruction of the bones is achieved by optimizing the model parameters to maximize the similarity between its rendered versions to the input X-ray images. Recently, [15] used a deep learning approach for detecting landmarks in X-ray images and triangulating them to 3D points. However, their network does not directly outputs bone reconstructions, and the detected 3D landmarks are only used to initialize a 3D deformable model. As a result, an SSM optimization is still required and takes around 1 minute.

**Reconstruction from multiple images** Several recent methods [24,26] use deep learning approaches for reconstructing a shape from single image, for predefined objects [27]. Geometrically, by using two or more images, it is possible to reconstruct a 3D surface by triangulating corresponding points, assuming the cameras' relative positions are known [11]. The relative poses of the cameras can be computed by matching points [20] or lines [28,14,2] descriptors. Several recent papers use deep learning approaches to reconstruct shapes from two and more images. 3D-R2N2 [4] and LSM [13] use RNNs to fuse feature from multiple images for reconstructing a binary voxels mask for representing 3D models. In contrast, [29] reconstructs one volume from each image and fuses them in a context-aware layer. [25] initializes a mesh from one of the views by [24] and refines it by repeatedly applying graph convolutional layers on its 3D coordinates with learned 2D features sampled from the projections of the 3D points on the multiple images. [3] uses deep network to reconstruct 3D models from simulated bi-planar X-ray images of a single spine vertebra by applying 2D convolutional layers to encode the images into a feature vector, and then decoding it to a 3D reconstruction using 3D convolutional layers. In contrast, our method uses more effective, and geometrically consistent network architecture that uses end-to-end 3D convolutional layers with skip connections, enabling faster and more accurate reconstruction of multi-class bones as we show in Sec. 4.2.

**Computed Tomography from X-ray images** Although mathematically, generation of computed tomography from few images is an ill-posed problem, a prior knowledge on the scanned objects can approximate the free parameters. X2CTGAN [30] uses an end-to-end deep learning approach for reconstructing a CT from X-ray images. [23] trains a patient-specific deep network to extract a CT volume from single X-ray image. [12] uses a deep network to reconstruct computed tomography of different mammalian species from single X-ray images. However, these approaches only estimate CT volumes, and another challenging segmentation step is required for extracting 3D reconstructions of the anatomical objects.

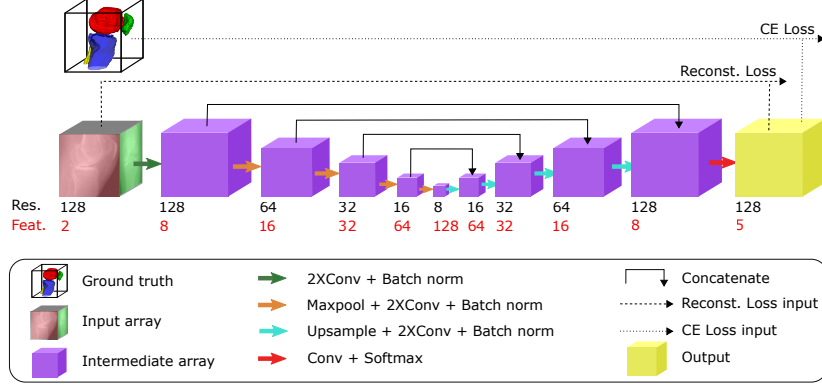


Fig. 2: Our deep network architecture and loss functions as described in Sec. 3.

## 3 Method

### 3.1 Network Architecture

Given two bi-planar X-ray images of lateral and Anterior-Posterior (AP) views, both of sizes  $128 \times 128$ , we first create a two channeled volume representation of size  $128 \times 128 \times 128$ . As illustrated in Fig.1, the volume has two channels, each contains one view ( lateral or AP) replicated 128 times over one dimension (0,1 respectively). Assuming that the input images are rectified orthographic projections from orthogonal views, each axial slice in this volume contains an epipolar plane, with voxels, back-projected from pixels of two corresponding epipolar lines. Therefore, this 3D representation is geometrically consistent with the input images.

The rest of the architecture is inspired by [21] and presented in Fig. 2. We use 3D convolutions of size  $3 \times 3 \times 3$ , and skip connections between the encoding and the decoding layers. The last layer is a  $1 \times 1 \times 1$  convolution block with 5 output channels, representing 5 output classes followed by a Softmax activation. Classes 0-4 represent an anatomical partitioning of the knee bones (see Fig. 3(e)).

### 3.2 Training

While CT images with ground truth 3D segmentation are available, pairs of X-ray images with associated ground truth 3D reconstructions are very rare. Moreover, geometrical alignment of each ground truth reconstruction with its X-ray images requires a 2D-3D registration process, which is itself challenging and error prone. Instead, we use annotated CT scans to create synthetic X-ray images by rendering DRRs. This way, each pair of synthetic X-ray images is associated with an aligned ground truth reconstruction.

For a supervised loss function, inspired by Fidel et al. [10] we spatially weight the cross-entropy loss to give more importance to the challenging near surface voxels. For each training sample, we define a spatial 3D Distance Weight Map

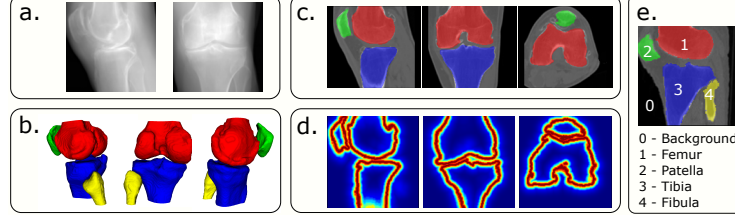


Fig. 3: Test set qualitative results for DRR input images (a-c), and training data visualization (d-e). (a) Biplanar input DRRs from the Test set. (b) Our reconstruction result from different view points. (c) Our reconstruction result displayed over a referenced CT scan, on 3 different axes. (d) Slices of Distance Weight Map (DWM) on 3 different axes. (e) Bone types and their assigned labels.

(DWM) that has a size of the ground truth volume where its value on voxel  $i$  is defined by:

$$DWM(i) = 1 + \gamma \cdot \exp(-d(i)/\sigma) \quad (1)$$

Where  $d$  is a distance transform that specifies for each voxel its corresponding distance from any bone surface, and  $\gamma, \sigma$  are constants which we set to 8, 10 respectively for all the training samples. A visual example is presented in Fig. 3(d). The DWM is then applied for weighting the voxel-wised cross entropy loss as follows:

$$loss_{CE} = -\frac{1}{N} \sum_{i=1}^N \sum_{k=0}^4 DWM(i) \cdot q_k(i) \cdot \log(p_k(i)) \quad (2)$$

where  $i$  is the index of a voxel,  $N$  is the total number of voxels,  $k$  is the class label,  $q_k(i) \in \{0, 1\}$  and  $p_k(i) \in (0, 1)$  are respectively the ground truth and network prediction probabilities of voxel  $i$  being labeled  $k$ .

We further define an unsupervised reconstruction loss to align the network prediction of bones probability map with the input X-ray images. Even though the input X-ray images contain bones together with additional anatomical elements, the image gradients of the bones are quite dominant. Therefore, the input X-rays are expected to have gradients that are relatively correlated with the DRRs from the predicted bones probability map.

The reconstruction loss is defined by:

$$Loss_{reconst} = 1 - \frac{1}{2} (NGCC(I_{Lat}, DRR_{Lat}) + (NGCC(I_{AP}, DRR_{AP}))) \quad (3)$$

where NGCC is the Normalized Gradient Cross Correlation<sup>1</sup>,  $I_{AP}, I_{Lat}$  are the input X-ray images from AP and lateral views respectively, and  $DRR_{AP}, DRR_{Lat}$  are DRRs applied on the maximum over the bones channels of the network prediction. This loss encourages the network to use the available

<sup>1</sup> The exact definition is given in the supplementary material

Table 1: Evaluation metrics for our results given inputs of bi-planar DRRs. The results are averaged over the test set of unseen 20 scans.

	Background	Femur	Patella	Tibia	Fibula	Bones average
Chamfer(mm)	-	1.075	1.709	1.175	1.218	1.294
Dice	0.986	0.943	0.894	0.945	0.848	0.907

information of the input images, that can actually be used in inference time, where no supervision is available. We observe that this loss improves the generalization of the network to unseen images (see Sec. 4.1). Overall our loss function is:

$$Loss = \frac{1}{2}(Loss_{reconst} + Loss_{CE}) \quad (4)$$

For training the network, Adam optimizer was used with initial learning rate of  $10^{-2}$ , divided by a factor of 10 every 10 epochs. We used training, validation and test sets of 188, 10 and 20 scans respectively, created from knee joint CT scans with associated GT segmentations and reconstructions. Each scan was augmented by rotating it randomly with random angles of range  $(-5, 5)$  and projected into 2 bi-planar DRRs which are used as synthetic input X-rays. We trained the network for 23 epochs.

### 3.3 Domain adaptation

X-ray images have a different appearance than DRRs. In order to apply our deep model on X-ray images, we trained a network that is based on CycleGAN [31] to transfer them to have a DRR-style appearance. During training, in each iteration the model uses two non aligned images  $I_{Xray}$  and  $I_{DRR}$  to generate two fake images:  $I_{DRR \rightarrow Xray}$ ,  $I_{Xray \rightarrow DRR}$ . In order to generate DRR-style images which are completely aligned with the input X-ray images we use the original CycleGAN with additional content preserving loss function:

$$L_{Cont} = 1 - \frac{1}{2}(ZNGCC(I_{Xray \rightarrow DRR}, I_{Xray}) + (ZNGCC(I_{DRR \rightarrow Xray}, I_{DRR})) \quad (5)$$

Where ZNGCC is the Zero Normalized Gradient Cross Correlation<sup>2</sup>. We trained the style transfer model with training/validation sets of 370/57 pairs of bi-planar X-ray images of the knee, for 30 epochs. In the supplementary material we show visual results of the style transfer process.

## 4 Experiments

### 4.1 DRR inputs

We tested our method on a test set of 20 scans (see Sec. 3.2), and evaluated the results using the ground truth 3D segmentations and reconstructions. Each pair

<sup>2</sup> The exact definition is given in the supplementary material

Table 2: Quantitative evaluation of real 28 test pairs of X-rays inputs, and comparisons with the femur reconstructions of [16] and [3]. The results are averaged over the test set. The patella metrics computed only on the lateral view (GT annotations for the AP view are unavailable).

	Femur SSIM [16]		[3]	Ours				
	Manual	Perturbed	Femur	Femur	Patella	Tibia	Fibula	Bones avg.
Chamfer(mm)	7.529	8.559	3.984	<b>1.691</b>	1.198	1.135	2.873	1.778
Dice	0.803	0.783	0.878	<b>0.948</b>	0.91	0.959	0.809	0.906

Table 3: Ablation study. Measuring the importance of different components of our model for real X-rays. The results metrics are averaged over the 4 reconstructed bones.

	Full	Without <i>DWM</i>	Lateral only	No $Loss_{reconst}$	No style transfer
Chamfer(mm)	<b>1.778</b>	1.863	2.979	1.92	6.146
Dice	<b>0.906</b>	0.901	0.844	0.892	0.742

of bi-planar DRRs is used as an input to our deep network described in Sec. 3.1. For each testing sample we used the Marching Cubes algorithm[19] to extract a set of 3D bones meshes from the predicted volumetric labels. A qualitative result is presented in Fig. 3a-3c. Quantitative metrics are calculated for each bone type and presented in Table 1. Dice (higher is better) is computed over the predicted voxels maps and Chamfer (lower is better) is computed directly on the final reconstructions.

## 4.2 Real X-ray test cases

We evaluated 28 test cases of X-ray images. Each pair of lateral and AP X-ray images was cropped manually by an expert to contain a bi-planar pair of rectified images of the knee joint such that, when resized to  $128 \times 128$  pixels, the pixel size is 1 mm. Even though the view directions of the X-ray images are not guaranteed to be exactly orthogonal, our method, trained on purely orthogonal inputs, handled such cases successfully. We applied domain adaptation procedure to transform their style as described in Sec. 3.3, and applied the network on the transformed X-ray images. In Fig. 4 we present a qualitative results of a 3D reconstruction given an input of bi-planar real X-ray images. Since 3D ground truth is not available for the X-ray images, we use 2D bi-planar ground truth multi-class masks annotated by experts for each case for evaluation: each reconstructed 3D model is projected to the 2 X-ray views and the evaluation metrics are computed relative to the GT masks.

We compare our performance with two baseline methods: the femur SSIM model<sup>3</sup> of [16], and the single bone reconstruction deep network of [3], trained

<sup>3</sup> Only their femur model has an available code

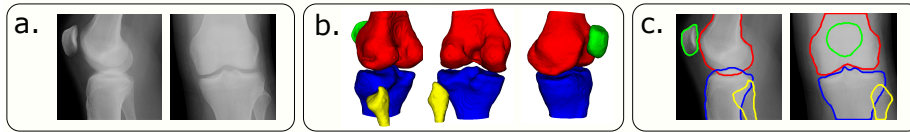


Fig. 4: Qualitative results on real X-rays. (a) Biplanar input X-rays. (b) 3D reconstruction result displayed from different view angles. (c) Boundaries of reconstruction projections displayed over the input X-rays .

using our training set for reconstructing the femur, and tested with the real X-ray test images (after applying our domain adaptation). Quantitative comparisons are presented in Table 2. Since [16] requires initialization for the SSIM model, we initialized it manually to the best of our ability. The optimization of [16] converged after 4.88 seconds, while our method, without any initialization reconstructs 4 bone types in 0.5 seconds, and achieves better results. Our method is more accurate and much faster than [3] which runs in 45 seconds for one bone reconstruction. To demonstrate the initialization sensitivity of [16], for each case of the test cases we applied a random perturbation on the manual initialization: we shifted the position parameters in a range of 20mm, multiplied the scale parameters by a factor of range  $[0.985, 1.015]$ , and evaluated the average results (see Table 2, "Perturbed"). The average running time for the perturbed initialization increased from 4.88 seconds to 6.05 seconds, while 34% of the perturbed cases did not converge at all. We further show an ablation study in Table 3 of running the model without several of its components to evaluate their importance.

*Technical details* We performed all of our experiments on a computer with MS Windows 10 64bit OS, Intel i7 7700K CPU and Nvidia GeForce GTX 1070 graphic card. The data is provided by a third party who has obtained consent for use in research.

## 5 Conclusion

We presented an effective end-to-end deep network for knee bones 3D reconstruction from bi-planar X-ray scans. We used a novel representation, training from synthetic data and domain adaptation to achieve an efficient, robust and accurate method. In the future we would like to extend our method to more bones reconstruction setups, and to extend the geometric 2D-3D representation of our model for additional X-ray projection models.

**Acknowledgements.** The authors thank Aliza Tarakanov, Arie Rond, Noy Moskovich, Eyal Shenkman, Eitan Yeshayahu, Yara Hussein, Astar Maloul-Zamir, Liam Simani, Polina Malahov and Amit Hadari M.D, for their help in datasets creation and annotation.

## References

1. Baka, N., Kaptein, B.L., de Bruijne, M., van Walsum, T., Giphart, J., Niessen, W.J., Lelieveldt, B.P.: 2d–3d shape reconstruction of the distal femur from stereo x-ray imaging using statistical shape models. *Medical image analysis* **15**(6), 840–850 (2011)
2. Ben-Artzi, G., Kasten, Y., Peleg, S., Werman, M.: Camera calibration from dynamic silhouettes using motion barcodes. In: *Proceedings of the IEEE Conference on Computer Vision and Pattern Recognition*. pp. 4095–4103 (2016)
3. Chen, C.C., Fang, Y.H.: Using bi-planar x-ray images to reconstruct the spine structure by the convolution neural network. In: *International Conference on Biomedical and Health Informatics*. pp. 80–85. Springer (2019)
4. Choy, C.B., Xu, D., Gwak, J., Chen, K., Savarese, S.: 3d-r2n2: A unified approach for single and multi-view 3d object reconstruction. In: *European conference on computer vision*. pp. 628–644. Springer (2016)
5. Cootes, T.F., Taylor, C.J., Cooper, D.H., Graham, J.: Active shape models-their training and application. *Computer vision and image understanding* **61**(1), 38–59 (1995)
6. Cresson, T., Branchaud, D., Chav, R., Godbout, B., de Guise, J.A.: 3d shape reconstruction of bone from two x-ray images using 2d/3d non-rigid registration based on moving least-squares deformation. In: *Medical Imaging 2010: Image Processing*. vol. 7623, p. 76230F. International Society for Optics and Photonics (2010)
7. Ehlke, M., Ramm, H., Lamecker, H., Hege, H.C., Zachow, S.: Fast generation of virtual x-ray images for reconstruction of 3d anatomy. *IEEE transactions on visualization and computer graphics* **19**(12), 2673–2682 (2013)
8. Fotsin, T.J.T., Vázquez, C., Cresson, T., De Guise, J.: Shape, pose and density statistical model for 3d reconstruction of articulated structures from x-ray images. In: *2019 41st Annual International Conference of the IEEE Engineering in Medicine and Biology Society (EMBC)*. pp. 2748–2751. IEEE (2019)
9. Goswami, B., Misra, S.: 3d modeling of x-ray images: A review. *Int. J. Comput. Appl* **132**(7), 40–46 (2015)
10. Guerrero-Pena, F.A., Fernandez, P.D.M., Ren, T.I., Yui, M., Rothenberg, E., Cunha, A.: Multiclass weighted loss for instance segmentation of cluttered cells. In: *2018 25th IEEE International Conference on Image Processing (ICIP)*. pp. 2451–2455. IEEE (2018)
11. Hartley, R., Zisserman, A.: *Multiple view geometry in computer vision*. Cambridge university press (2003)
12. Henzler, P., Rasche, V., Ropinski, T., Ritschel, T.: Single-image tomography: 3d volumes from 2d cranial x-rays. In: *Computer Graphics Forum*. vol. 37, pp. 377–388. Wiley Online Library (2018)
13. Kar, A., Häne, C., Malik, J.: Learning a multi-view stereo machine. In: *Advances in neural information processing systems*. pp. 365–376 (2017)
14. Kasten, Y., Ben-Artzi, G., Peleg, S., Werman, M.: Fundamental matrices from moving objects using line motion barcodes. In: *European Conference on Computer Vision*. pp. 220–228. Springer (2016)
15. Kim, H., Lee, K., Lee, D., Baek, N.: 3d reconstruction of leg bones from x-ray images using cnn-based feature analysis. In: *2019 International Conference on Information and Communication Technology Convergence (ICTC)*. pp. 669–672. IEEE (2019)

16. Klima, O., Kleparnik, P., Spanel, M., Zemcik, P.: Gp-gpu accelerated intensity-based 2d/3d registration pipeline. In: Proceedings of Shape Symposium. Delemont: Swiss Institute for Computer Aided Surgery (2015)
17. Lamecker, H., Wenckebach, T.H., Hege, H.C.: Atlas-based 3d-shape reconstruction from x-ray images. In: 18th International Conference on Pattern Recognition (ICPR'06). vol. 1, pp. 371–374. IEEE (2006)
18. LeCun, Y., Bengio, Y., Hinton, G.: Deep learning. *nature* **521**(7553), 436–444 (2015)
19. Lorensen, W.E., Cline, H.E.: Marching cubes: A high resolution 3d surface construction algorithm. *ACM siggraph computer graphics* **21**(4), 163–169 (1987)
20. Lowe, D.G.: Distinctive image features from scale-invariant keypoints. *International journal of computer vision* **60**(2), 91–110 (2004)
21. Milletari, F., Navab, N., Ahmadi, S.A.: V-net: Fully convolutional neural networks for volumetric medical image segmentation. In: 2016 Fourth International Conference on 3D Vision (3DV). pp. 565–571. IEEE (2016)
22. Reyneke, C.J.F., Lüthi, M., Burdin, V., Douglas, T.S., Vetter, T., Mutsvangwa, T.E.: Review of 2-d/3-d reconstruction using statistical shape and intensity models and x-ray image synthesis: Toward a unified framework. *IEEE reviews in biomedical engineering* **12**, 269–286 (2018)
23. Shen, L., Zhao, W., Xing, L.: Patient-specific reconstruction of volumetric computed tomography images from a single projection view via deep learning. *Nature biomedical engineering* **3**(11), 880–888 (2019)
24. Wang, N., Zhang, Y., Li, Z., Fu, Y., Liu, W., Jiang, Y.G.: Pixel2mesh: Generating 3d mesh models from single rgb images. In: Proceedings of the European Conference on Computer Vision (ECCV). pp. 52–67 (2018)
25. Wen, C., Zhang, Y., Li, Z., Fu, Y.: Pixel2mesh++: Multi-view 3d mesh generation via deformation. In: Proceedings of the IEEE International Conference on Computer Vision. pp. 1042–1051 (2019)
26. Wu, J., Wang, Y., Xue, T., Sun, X., Freeman, B., Tenenbaum, J.: Marrnet: 3d shape reconstruction via 2.5 d sketches. In: Advances in neural information processing systems. pp. 540–550 (2017)
27. Wu, Z., Song, S., Khosla, A., Yu, F., Zhang, L., Tang, X., Xiao, J.: 3d shapenets: A deep representation for volumetric shapes. In: Proceedings of the IEEE conference on computer vision and pattern recognition. pp. 1912–1920 (2015)
28. Wurfl, T., Aichert, A., Maass, N., Dennerlein, F., Maier, A.: Estimating the fundamental matrix without point correspondences with application to transmission imaging. In: The IEEE International Conference on Computer Vision (ICCV) (October 2019)
29. Xie, H., Yao, H., Sun, X., Zhou, S., Zhang, S.: Pix2vox: Context-aware 3d reconstruction from single and multi-view images. In: Proceedings of the IEEE International Conference on Computer Vision. pp. 2690–2698 (2019)
30. Ying, X., Guo, H., Ma, K., Wu, J., Weng, Z., Zheng, Y.: X2ct-gan: reconstructing ct from biplanar x-rays with generative adversarial networks. In: Proceedings of the IEEE conference on computer vision and pattern recognition. pp. 10619–10628 (2019)
31. Zhu, J.Y., Park, T., Isola, P., Efros, A.A.: Unpaired image-to-image translation using cycle-consistent adversarial networks. In: Proceedings of the IEEE international conference on computer vision. pp. 2223–2232 (2017)

## A Supplementary Material

$$NGCC(I_1, I_2) = \frac{1}{2} \left( \frac{G_x(I_1)}{\|G_x(I_1)\|} \cdot \frac{G_x(I_2)}{\|G_x(I_2)\|} + \frac{G_y(I_1)}{\|G_y(I_1)\|} \cdot \frac{G_y(I_2)}{\|G_y(I_2)\|} \right) \quad (6)$$

$$\overline{G_x(I)} = G_x(I) - \text{mean}(G_x(I)), \overline{G_y(I)} = G_y(I) - \text{mean}(G_y(I)) \quad (7)$$

$$ZNGCC(I_1, I_2) = \frac{1}{2} \left( \frac{\overline{G_x(I_1)}}{\|\overline{G_x(I_1)}\|} \cdot \frac{\overline{G_x(I_2)}}{\|\overline{G_x(I_2)}\|} + \frac{\overline{G_y(I_1)}}{\|\overline{G_y(I_1)}\|} \cdot \frac{\overline{G_y(I_2)}}{\|\overline{G_y(I_2)}\|} \right) \quad (8)$$

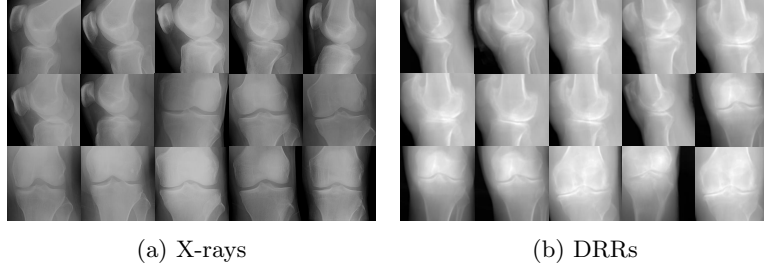


Fig. 5: Visualization of the training data that we used for training CycleGAN.

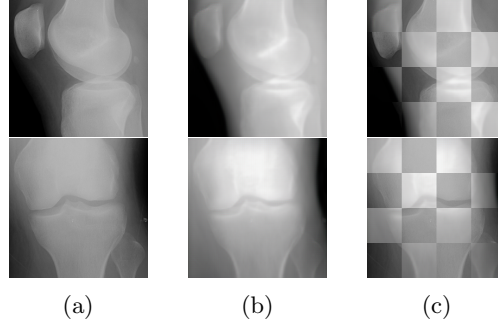


Fig. 6: CycleGAN results: (a) X-ray inputs. (b) DRR-style outputs. (c) Inputs-outputs content comparisons.

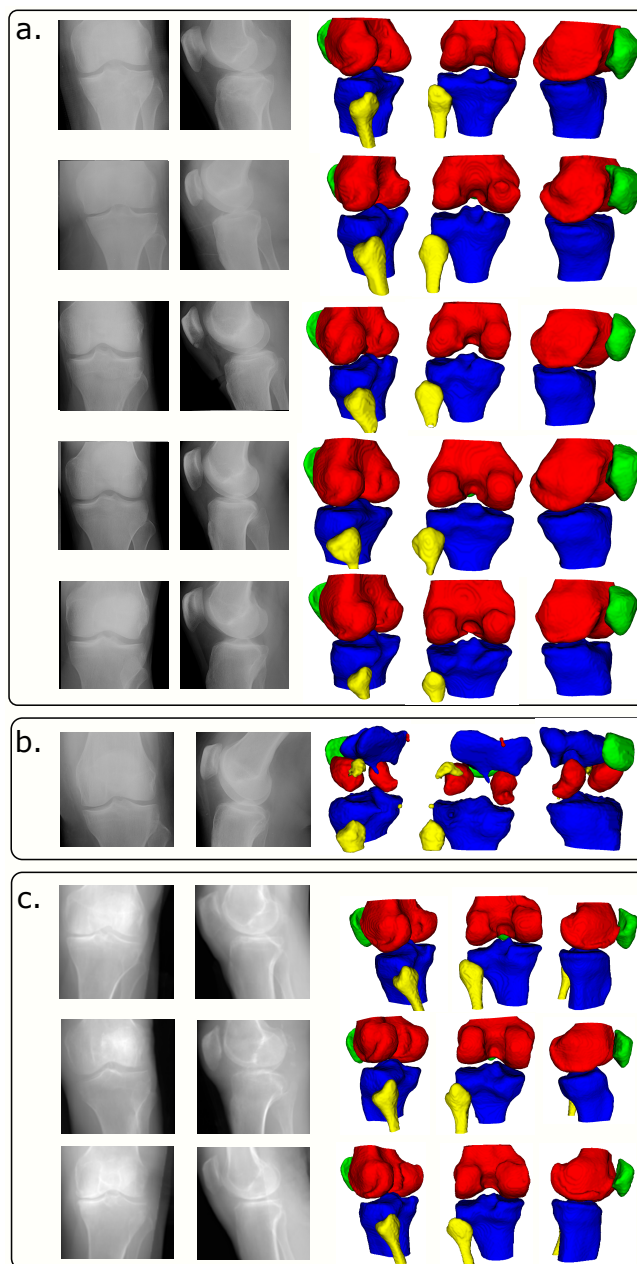


Fig. 7: Supplementary qualitative results on test cases: left - inputs, right - outputs. (a) Real X-rays inputs. (b) Real X-rays inputs without Cycle-GAN, as ablation study. (c) DRRs inputs.